Particle size distribution effects in an FEM model of sintering porous ceramics

Darcovich, Kenneth; Béra, Laurent; Shinagawa, Kazunari

Publisher's version / Version de l'éditeur:
https://doi.org/10.1016/S0921-5093(02)00237-X
Materials Science and Engineering A, 341, January, pp. 247-255, 2003

ELSEVIER

Materials Science and Engineering A341 (2003) 247–255

MATERIALS SCIENCE & ENGINEERING A

www.elsevier.com/locate/msea

Particle size distribution effects in an FEM model of sintering porous ceramics[1]

Ken Darcovich [a,*], Laurent Béra [b], Kazunari Shinagawa [c]

[a] Institute for Chemical Process and Environmental Technology, National Research Council of Canada, Ottawa, ON, Canada K1A 0R6
[b] Institut Catholique d'Arts et Métiers, 6, rue Auber, 59046 Lille Cedex, France
[c] Department of Advanced Materials Science, Faculty of Engineering, Kagawa University, Hayashi-cho 2217-20, Takamatsu 761-0396, Japan

Abstract

A numerical simulation is presented on the sintering of porous alumina structures prepared by a controlled sedimentation technique. By forming this functionally gradient material with a very broad powder size distribution, the samples were able to remain flat through sintering. This experimental result is reflected in the present simulation results, which incorporated particle size distribution effects. In general, sintering functionally gradient ceramics can often introduce defects. Despite these common problems, the asymmetric structures considered in this paper featured a vertical functionality of continuously overlapping broad powder size distributions in the structure. This arrangement served to homogenize sintering rates. Modelling presented in connection with this shows that such structures can be readily sintered without warpage or cracking. To demonstrate these effects, a finite element method numerical simulation was developed to model the sintering characteristics of porous asymmetric ceramic structures by incorporating the powder particle size distribution into the model as a field variable. This work presents novel advances in the sintering model such that the contributions to the desired product properties attributable to particle size distribution effects can be demonstrated. These additions to the model produce numerical results which properly match observed structural profiles of physical samples.

Keywords: Porous ceramics; FEM model; Sintering; Particle size distribution

1. Introduction

As part of an on-going project, porous structures expressly intended as membrane substrates have been prepared via a polydisperse slurry sedimentation method which yields a functionally gradient material. The benefit of creating an asymmetric microstructure is to produce a smaller substrate pore size over a thinner region, thereby imparting superior permeation properties.

Preliminary work demonstrated the viability of this method for preparing functionally gradient samples made from α-alumina which retain a high porosity after sintering [1]. SEM images demonstrated the continuously increasing mean particle size across the cross-section of the samples [2]. Experimentally, it was found that warping and cracking problems in functionally gradient materials could be resolved by producing a structure with continuously overlapping particle size distributions in the vertical direction [3]. This served to homogenize sintering rates and allowed the asymmetric compacts to remain flat while sintering. In view of this, it is the objective of this paper to extend a constitutive sintering model to incorporate the effects of the particle size distribution as a local field variable. In this way it is possible to demonstrate the crucial differences which arise during sintering from particle interactions within a broad distribution, instead of simply considering mean powder properties. This paper addresses how some of the unique properties of these functionally gradient structures influence their sintering behaviour.

In the literature a number of basic models have been developed to describe the fundamental point of contact sintering models at work. Abouaf et al. formulated rate forms of constitutive equations of visco-elastic type to

* Corresponding author. Tel.: +1-613-993-6848; fax: +1-613-941-2529

E-mail address: ken.darcovich@nrc.ca (K. Darcovich).

[1] NRCC No. 44380.

0921-5093/02/$ - see front matter
PII: S0921-5093(02)00237-X

simulate the sintering and densification of metal powders [4]. This work dealt with component fabrication by hot isostatic pressing. A similar model was also presented by Riedel et al. with emphasis on shear and friction forces which occur in component densification [5].

A paper by Jagota and Scherer modelled sintering of composite packings of spheres [6]. This model is relevant to the present work with porous functionally gradient materials in that differential sintering rates were integral to successful treatment of the sample. In their case, the simulation made use of a discrete model of 1146 particles.

A number of microscopic models of sintering based on grain boundary diffusion mechanisms have been presented [7–9]. Mass transfer at interparticle contacts provides a basis for extending the models to a macroscopic scale. In particular, the Shinagawa model available for the present work, has been adapted to treat porous functionally gradient materials in the early stages of sintering. It was used to obtain a good correspondence with experimental densification measurements with alumina samples, relevant to our present work [10]. In [10] this model was compared to constitutive formulations by Ashby [11], McMeeking and Kuhn [8] and Svoboda et al. [12], where differences and rationale for its suitability for the sintering of alumina were given.

Until now, no models have been formulated which explicitly account for particle size distribution effects. Sintering simulations of FGMs have only been realized by imparting mean powder properties [13–15]. It has been shown experimentally however, that local distribution effects can override tendencies that would otherwise be predicted considering only mean powder properties. It therefore is the main objective of this paper to detail formulations related to particle size distribution effects, and incorporate them into a finite element method simulation of sintering to demonstrate that these features are necessary for obtaining qualitative output corresponding to experimental results.

2. Original constitutive model for sintering

Sintering can be regarded as the process whereby a particle agglomerate is transformed into a porous body which may be considered as a continuum. Elevated temperatures and the accompanying grain growth may promote this transformation. A constitutive model for sintering can be expressed as,

$$\dot{\varepsilon}_{ij} = \frac{\sigma'_{ij}}{2G} + \delta_{ij}\frac{\sigma_m - \sigma_s}{3K}, \tag{1}$$

or,

$$\dot{\varepsilon}_{ij} = \frac{1}{2\eta}[C\sigma'_{ij} + F(\sigma_m - \sigma_s)\delta_{ij}], \tag{2}$$

where $\dot{\varepsilon}$ is the strain rate, σ' is the deviatoric stress, σ_m is the hydrostatic stress, σ_s is the sintering stress and η is the shear viscosity term for full density. G and K or C and F are parameters representing the relative density dependent viscosity. Establishing the constitutive model consists of identifying G and K or C and F as well as σ_s as a function of the relative density and grain size. Parhami and McMeeking computed the values of these parameters for the initial stage of sintering by a discrete element network method [16]. However, their simulations are performed only for monosize spherical powder particles because the discrete element method lacks general models for the growth of interparticle contact and shrinkage between different sized particles in the process of coarsening. Shinagawa and Hirashima presented the functions for C, F and σ_s in a constitutive model, developed for the intermediate stage of sintering, treating a sintering body as a porous crystalline body consisting of monosize grains undergoing coarsening [15]. Although the present process may be dominated by the early stage of sintering, we apply the existing functions for C, F and σ_s to examine the effects of particle size distribution and its evolution by coarsening on the viscosity. That is, the objective of the present study was not to focus on the parameter values themselves. The basic functional equivalence of Eqs. (1) and (2) allows the use of this kind of model for treating polycrystalline material with what appears to be a viscous sintering model. Naturally, a fully rigorous and mechanistic simulation is not claimed in this case, rather it is suggested that the available model and code employed here are at least suitable as a tool for demonstrating particle size distribution effects in the sintering of asymmetric porous structures.

Some details of this constitutive model are outlined below. Two main aspects are considered: first, the basic equations with grain boundary diffusion and grain growth are given, and secondly, a model for microscopic shrinkage is presented.

2.1. Sintering strain and stress relation

As derived previously [9], the constitutive strain equation for the strain rate $\dot{\varepsilon}_{ij}$, is,

$$\dot{\varepsilon}_{ij} = \frac{1}{2\eta}\frac{1}{\rho^{2n-1}}\left\{\sigma'_{ij} + \delta_{ij}\frac{2}{9f^2}(\sigma_m + \sigma_s)\right\}, \tag{3}$$

where,

$$f = 1/(2.5\sqrt{1-\rho}) \quad n = 2.5 \quad \text{and} \quad i, j = x, y, z.$$

The factor f in Eq. (3) represents the degree of the hydrostatic stress component. An expression for the

sintering stress is given below,

$$\sigma_s = \rho^N \frac{2\gamma}{\zeta R}\left\{\frac{\rho}{\rho_0}\frac{(1-\rho_0)^{1/3}}{(1-\rho)}\right\}, \tag{4}$$

where, γ is the solid surface tension, R is the particle radius and ρ_0 is the initial relative density. ζ and N are constants, given as 0.5 and 5, respectively [10]. Note that the sintering stress in the present formulation derives from the plasticity theory of Shima and Oyane [17], where compression was taken to be positive, since this is the main process for porous bodies. This is the opposite of conventional expressions for σ_s.

2.1.1. Grain boundary diffusion

Using a result from Coble [18] as the basis for the deformation rate for grain boundary diffusion, an expression for the viscosity term can be obtained,

$$\eta = \frac{\sigma}{3\dot{\varepsilon}} = \frac{1}{3}\frac{kTd^3}{47\ \Omega h D_b}. \tag{5}$$

In Eq. (5), Ω is the atomic volume, h is the width of the grain boundary, D_b is the grain boundary diffusion coefficient, k is Boltzmann's constant, T is the absolute temperature and d is the grain size. The temperature dependence of the diffusion coefficient follows the exponential model,

$$D_b = D_0 \exp\left(\frac{-Q_d}{kT}\right), \tag{6}$$

where D_0 is the frequency term and Q_d is the activation energy of grain boundary diffusion. Parameter values were determined experimentally by creep testing [19].

2.1.2. Surface tension

The solid surface tension as a function of temperature is given by,

$$\gamma = \gamma_0 + aT \quad (\text{mN m}^{-1}). \tag{7}$$

Kingery [20] found Eq. (7) parameter values for alumina to be $\gamma_0 = 1117$ mN m^{-1}, and $a = -0.1$ with T in (K).

3. Sintering deformation analysis

The finite element numerical method is employed to apply the constitutive model developed above. This simulation can be used in a predictive manner to assess time–temperature profiles for sintering of porous ceramics. Modifications to the basic model given above, to input the local effects related to particle size distribution were formulated and implemented to show how the presence of fines throughout the entire structure could reduce the extent of warpage. Small particles from the fines tail of a distribution, in contact with any other size class, should begin sintering at lower temperatures than particles corresponding to the mean diameters across the vertical range of the functionally gradient structure.

3.1. Finite element sintering simulation

The flow stress of powder particles during sintering can be expressed from Eq. (3) to Eq. (5), leading to a matrix form of the stress–strain rate relations, whose details are given fully elsewhere [15].

The physical domain undergoing sintering can be discretized in a rectangular type grid shown in Fig. 1. In this case, what is treated is a two dimensional cross-section of a disc which is 45 mm in diameter and 3.3 mm thick. Through symmetry, only half of the structure is considered in the horizontal direction. This cross-section is represented by a grid composed of 10 elements in the vertical direction and 34 elements in the horizontal direction. As the simulation proceeds, the grid is deformed according to strain rates calculated at each time step. Grid refinement was not considered, as the objective of the work was to illustrate mechanisms providing rationale for results which are qualitatively quite different for two different cases, rather than to demonstrate numerical precision and/or accuracy.

The internal microscopic changes occurring locally during sintering contribute to the overall macroscopic shape transition of the ceramic piece. The finite element simulation provides this information by inserting the effective sintering stresses σ_s from Eq. (4) and the apparent viscosity η from Eq. (5) into the overall force balance. Subsequently, the hydrostatic stress component and the shrinkage rate in each grid element are calculated by Eqs. (3) and (4) along with the nodal force balances. This enables a determination of the changes in density and volume. The time step used in the simulation is 1 min, which gives sufficient smoothness and resolution of results. With updated density and volume values, the calculation as outlined above can be repeated and marched forward in time according to the prescribed sintering time–temperature profile.

4. Formulations to account for particle size distributions

4.1. Evolution of a grain size distribution under sintering

A distribution of grain sizes undergoing sintering will evolve over time as finer particles are consumed in order for larger ones to grow. A population balance conserving overall system volume was employed by Sivakumar

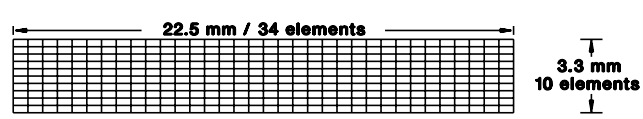

Fig. 1. FEM grid used for numerical simulations.

et al. [21], derived from the original more general case developed by Hulburt and Katz [22]. The relationship between the particle radius r and its frequency in a distribution $\mathscr{F}$ is,

$$\frac{\partial \mathscr{F}}{\partial t} + \frac{\partial}{\partial r}(v_r \mathscr{F}) = 0. \tag{8}$$

Above, the term v_r is known as a grain growth velocity function, expressed as,

$$v_r = \frac{dr}{dt} = \frac{C_G}{r^n}\left(\frac{1}{r_c} - \frac{1}{r}\right), \tag{9}$$

where C_G is a sintering parameter of units ($m^{n+1}\ s^{-1}$), and n is an exponent which depends on the mechanism of grain growth. $n = 0$, 1, or 2 for surface diffusion, bulk diffusion or diffusion by dislocation, respectively. The parameter r_c is an instantaneous critical radius in the distribution with zero growth. That is, particles with a larger radius grow, while particles with a lesser radius shrink. For grain boundary diffusion, r_c can be calculated from a ratio of distribution moments. Details of this calculation are given in Ref. [21]. As the simulation advances, r_c is recalculated at each time step, and in general it increases in value as the sintering proceeds. Eq. (8) assumes grain growth proceeds independently of pore shrinkage and the sample is spatially homogeneous. For the ceramic bodies under consideration here, this requires making use of a local particle size distribution at each node in the body.

Substitution of Eq. (9) into Eq. (8) yields,

$$\frac{\partial \mathscr{F}}{\partial t} + \frac{\partial}{\partial r}\left(\frac{C_G \mathscr{F}}{r^n}\left(\frac{1}{r_c} - \frac{1}{r}\right)\right) = 0. \tag{10}$$

Eq. (10) can be transformed by the method of characteristics into two ordinary differential equations, to enable each radius r and its corresponding frequency $\mathscr{F}$ to be solved together in a marching algorithm. For r, Eq. (9) is simply employed, and for $\mathscr{F}$, as shown by Sivakumar et al. [21],

$$\frac{d\ln \mathscr{F}}{dt} = \frac{C_G}{r^{n+1}}\left(\frac{n}{r_c} - \frac{n+1}{r}\right). \tag{11}$$

Numerically, Eqs. (9) and (11) can be solved by discretizing a particle size distribution and marching forward in small time steps. The IMSL routine IVPAG was used to accomplish this.

Results from a theoretical and experimental study by Ting and Lin [23] were used to assign a numerical value to C_G for the sintering of alumina. Using densification rate data, and a formula derived relating C_G, density and sintering time, it was possible to calculate an estimate of C_G at 1500 °C as 0.02283 $\mu m^3\ min^{-1}$ for the grain boundary diffusion case. This value is of a similar order of magnitude as the example parameter (0.01) used by Sivakumar et al. [21].

The theoretical basis for the parameter C_G was formulated by Greenwood [24]. It can be written as,

$$C_G = \frac{2D_b S\gamma h}{kT}. \tag{12}$$

Above, the term S comes from the solubility in a particle of infinite radius (in the sense of diffusion), based on the Thomson–Freundlich equation, in refence to the sintering system comprising only solid and gas. Most of the parameters in Eq. (12) show only a weak dependence on temperature, such that it is plausible to estimate a temperature functionality based on a straight proportionality, so that,

$$C_G(T) = C_{G_{1500\ °C}}\left(\frac{D_b(T)}{D_b(1500\ °C)}\right)\left(\frac{1873.15}{T + 273.15}\right). \tag{13}$$

4.2. Distribution-based sintering strain coefficient calculation

The overall sintering rate is directly linked to the strain rate which arises during the sintering process. A paper by Pan et al. [25] details solid state diffusion between particles of different sizes under sintering conditions, and is also fundamentally based on Coble's model. In this case, the fusion of two adjoining particles via grain boundary diffusion was modelled. Grain boundary diffusion, which is the primary mechanism of reaction in the earlier stages of sintering, can be assumed to be the primary mechanism for the samples under consideration here. That is, the samples considered here are comparatively porous in the green state and they do not densify to the point where they are in a fused compact state. The original inter-particle points of contact remain after sintering, with neck regions still identifiable.

The model employed makes an assumption that grain growth is independent of pore shrinkage. It is known that the pinning of grain boundaries at necks plays a key role in grain growth, but in the present case, fairly porous structures are considered in what are essentially the initial stages of sintering. This simulation is a first attempt to demonstrate the effect of particle size distributions on the sintering of porous functionally gradient materials, so while those assumptions may limit the accuracy of the results, they do at the same time allow some of the features of sintering broad particle size distributions to be illuminated. In the same light, given the extent of the sintering, Fig. 6 suggests that identifying particle size with grain size is not unreasonable for the present purposes.

An expression for the reference strain rate, $\dot{\varepsilon}_{gb}$, was given, with r_b as the base particle radius.

$$\dot{\varepsilon}_{gb} = \frac{D_b h \Omega}{kT} \frac{\gamma}{r_b^4}. \tag{14}$$

The reference strain rate refers to an interaction of two like-sized particles of radius r_b. To account for particle pairs of differings sizes, an integration must be done considering the range of particle sizes and their relative frequencies of occurrence. For particles of two different sizes, r_i and r_b, an expression for the time required for the grain boundary to completely disappear t_d, was empirically determined as [25],

$$t_d = 0.15 \frac{kT}{\Omega \gamma_s D_b h} \left(\frac{D_b h}{D_s \delta_s}\right)^{0.85} \left(\frac{\gamma_{gb}}{\gamma}\right) \left(\frac{r_i}{r_b}\right)^{4.63} r_b^4. \tag{15}$$

Above, D_s is the surface diffusion coefficient, δ_s is the surface diffusion layer thickness, and γ_{gb} is the grain boundary interfacial tension. Eq. (15) has a bearing on the strain rate via the particle size ratio. If a shorter sintering time can be achieved, it must be done with a larger sintering strain. Since Eqs. (14) and (15) are both derived from Coble's theory, and have parallel functional forms containing many of the same coefficients, it can be postulated that,

$$\dot{\varepsilon}_{gb} \propto \frac{1}{t_d} \quad \text{or} \quad \dot{\varepsilon}_{gb} \propto K_M \frac{r_b^{0.63}}{r_i^{4.63}}.$$

The coefficient K_M is the product of the materials related parameters from Eq. (14). The purpose of this development is to expand the strain rate expression from Eq. (14) to include the effect of a particle pair as opposed to a single particle size. Eq. (14) is a rate expression as is Eq. (15). Figure 10 in Pan's original paper [25] shows a calculation for a wide range of ratios of surface to grain boundary diffusivities, and in all cases the slopes are the same, only relative absolute values change. Further, these calculations also include a case with $D_b \gg D_s$, suggesting that it would be appropriate to employ elements of this formulation in a model which does not include surface diffusion. In this sense, the unequal pair interaction is essentially defined by the exponent on the particle radius ratio term, and on this basis is thus employed in the present model for pair interaction effects. Let us now use the above result to rewrite Eq. (14) to incorporate the effects of the fusion on a reference or base size particle (r_b) with any other size class (r_i). Thus,

$$\dot{\varepsilon}_{gb}(r_i,\ r_b) = K_M \frac{r_b^{0.63}}{r_i^{4.63}}. \tag{16}$$

For the case where $r_b = r_i$, Eq. (16) reduces to Eq. (14). It can be seen that when $r_b > r_i$, the value of $\dot{\varepsilon}_{gb}$ increases, and would be reflected in a more rapid sintering in an object compared to one containing only particles of size r_b. The formulation is written such that the ratio r_i/r_b must be less than or equal to 1. One of the interesting consequences from Eq. (15) is that it can be shown that sintering is most accelerated for pairs with large size disparity. Fig. 2 shows a schematic for the various sintering rates which arise for the three possible pairings available with two different sized particles.

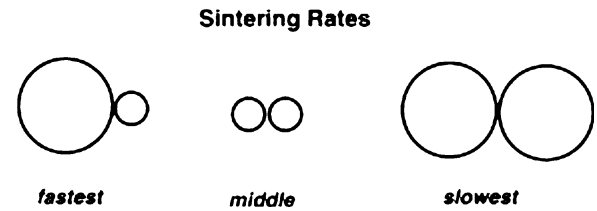

Fig. 2. Relative sintering rates of pair arrangements.

Note now that Eq. (16) contains effects brought about by pairs of particles of different sizes. To incorporate the effects of a particle size distribution, integration over weighted pairings across the distribution must be done to calculate a modifying coefficient for $\dot{\varepsilon}$. A further effect will be brought about by the local coordination number, or number of inter-particle points of contact in the body. A factor is employed as a ratio of the local particle size distribution-based coordination number ($C_{N_{PSD}}$) against a coordination number for a randomly packed structure of uniform particles ($C_{N_{AVG}}$). This would account for modified sintering rates arising from either more or fewer points of contact which are simultaneously contributing to the sintering of the body. For broad and continuous particle size distributions, Suzuki and Oshima [26] determined C_N as a function of an Andreasen distribution exponent, and the result was always approximately 6. For standard random packing of monosize spheres, $C_N \simeq 8$ [27]. Thus for the simulation conducted here the ratio of $C_{N_{PSD}}$ to $C_{N_{AVG}}$ was simply set to 0.75.

We introduce a new sintering strain $\dot{\varepsilon}_{PSD}$, to be used as indicated in Eq. (5), but accounting for local particle size distribution characteristics. Thus,

$$\dot{\varepsilon}_{PSD} = \left(\frac{\int_{r_S}^{r_L}\int_{r_S}^{r_b} \dot{\varepsilon}_{gb}(r_i,\ r_b)\, \mathscr{F}(r_i)\mathscr{F}(r_b)\ \mathrm{d}r_i\ \mathrm{d}r_b}{\int_{r_S}^{r_L}\int_{r_S}^{r_b} \mathscr{F}(r_i)\mathscr{F}(r_b)\ \mathrm{d}r_i\ \mathrm{d}r_b} \right) \times \left(\frac{C_{N_{PSD}}}{C_{N_{AVG}}}\right). \tag{17}$$

Above $\mathscr{F}(r_i)$ refers to the number freqency of particles of size class i in the particle size distribution.

In terms of the numerical implementation of Eq. (17), the FEM simulation makes use of Eqs. (3) and (5) to calculate $\dot{\varepsilon}$ via η. From Eq. (5), we can state,

$$\eta \propto \frac{1}{\dot{\varepsilon}} \propto t_d.$$

From Eq. (5) (reducing all constants into the parameter K_E) we have,

$$\eta = K_E d^3. \tag{18}$$

To introduce the effect of particle pairs into Eq. (18), we can replace d with the r_i/r_b ratio and the attendant functionality to reduce the expression back to its original state for the case when $r_i = r_b$. Thus,

$$\eta(r_i,\ r_b) = K_E\left(\left(\frac{(2r_i)^{4.63}}{(2r_b)^{0.63}}\right)^{1/4}\right)^3 = 8K_E\frac{r_i^{3.4725}}{r_b^{0.4725}}. \tag{19}$$

Finally, to then account for all pair interactions throughout the entire particle size distribution, an integration based on the statistical probability of all pair interactions such as used by Ting and Lin [23] is employed. Eq. (20) given below is used directly in the FEM simulation.

$$\eta_{PSD} = \left(\frac{\int_{r_S}^{r_L}\int_{r_S}^{r_b} \eta(r_i,\ r_b)\ \mathscr{F}(r_i)\mathscr{F}(r_b)\ \mathrm{d}r_i\ \mathrm{d}r_b}{\int_{r_S}^{r_L}\int_{r_S}^{r_b} \mathscr{F}(r_i)\mathscr{F}(r_b)\ \mathrm{d}r_i\ \mathrm{d}r_b}\right)\left(\frac{C_{N_{AVG}}}{C_{N_{PSD}}}\right)$$

$$= 8K_E\left(\frac{\int_{r_S}^{r_L}\int_{r_S}^{r_b} (r_i^{3.4725}/r_b^{0.4725})\ \mathscr{F}(r_i)\mathscr{F}(r_b)\ \mathrm{d}r_i\ \mathrm{d}r_b}{\int_{r_S}^{r_L}\int_{r_S}^{r_b} \mathscr{F}(r_i)\mathscr{F}(r_b)\ \mathrm{d}r_i\ \mathrm{d}r_b}\right)$$

$$\times\left(\frac{C_{N_{AVG}}}{C_{N_{PSD}}}\right). \tag{20}$$

Above, the factor from the effect of coordination number has been inverted, since η operates in a reciprocal fashion for determining the sintering strain rate.

To have an estimate of the effect of considering a particle size distribution rather than a mean diameter, the ratio of $\eta_{PSD}/\eta_{\bar{d}}$ is plotted against σ_N, a normalized standard deviation of a Gaussian distribution, defined as $\sigma/\bar{d}$. When the volume frequency is considered (Fig. 3), $\eta_{PSD}/\eta_{\bar{d}}$ levels off around 0.65 as σ_N increases, corresponding to more rapid sintering occurring in powder compacts made from broader particle size distributions.

4.3. Density evolution

The evolution of relative density in each region is calculated with Eq. (4). In this case, σ_m was set to zero, since no external stresses would be generated in these flat disc shaped specimens while sintering. The initial local pore size is the principal distinction in the sintering stresses found in each region. This is reflected by the parameter ζ which appears in Eq. (4). Larger ζ values correspond to larger pore sizes. Porosimetric measurements on powder compacts can supply the ρ_{i0} parameters.

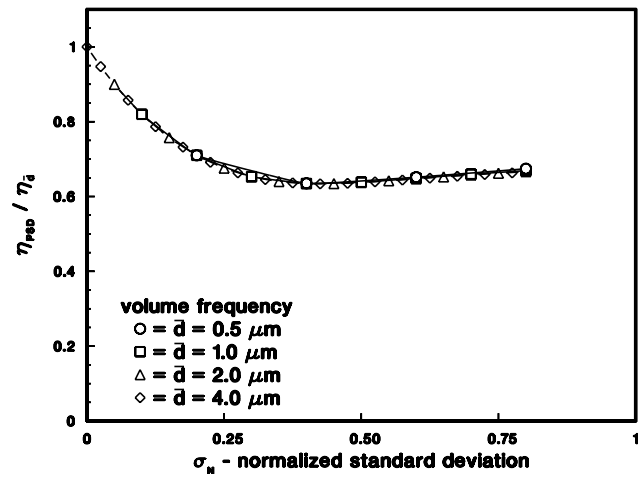

Fig. 3. $\eta_{PSD}/\eta_{\bar{d}}$ vs. σ_N for volume frequencies.

4.4. Sintering time–temperature profile

The time–temperature sintering profile used for these simulations is shown in Fig. 4. As boundary conditions, the outside surface temperature of the structure was considered to be equal to the temperature according to the sintering time–temperature profile. As an initial condition, the entire structure was considered to be at 20 °C at the start of the sintering program. Consequently, during heating the sample interior is cooler than the outside surface, and later during cooling, it is warmer.

In order to allow the simulation parameters to manifest themselves in a two-dimensional fashion, it was necessary to introduce a temperature field over the sample domain in the simulation. Without a temperature field which of course varies in two directions, the

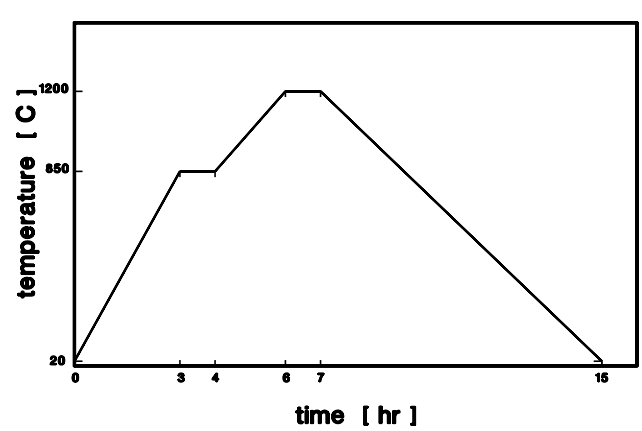

Fig. 4. Ramp and soak sintering profile.

microstructural properties in the sample would only show a variation in the vertical direction, since no other parameters are functions of y-position. Property variations in two directions would give a better representation of deformation, shrinkage and/or warpage. For a rectangular slab, heating by conduction was considered. The well known conduction equation, given below was employed.

$$\frac{\partial^2 T}{\partial x^2}+\frac{\partial^2 T}{\partial y^2}=\frac{\rho c}{k_T}\frac{\partial T}{\partial t}. \tag{21}$$

Above, x and y refer to horizontal and vertical coordinates, respectively, c is the heat capacity and k_T is the thermal conductivity. Data from the literature was found for alumina for c and k_T across the relevant temperature range [28,29]. The temperature field was solved by a finite element routine.

5. Results and discussion

The formulations as described above were coded for numerical implementation by the finite element method. The material under consideration was α-alumina in particulate form, consolidated into flat discs 45 mm in diameter and 3.3 mm thick. The structures were given a functionally gradient cross-section, with increasingly larger mean particle diameters occurring from the top to the bottom of the structure, in the range of 3–7 μm. Correspondingly, the porosity of the structure was set to vary linearly from 0.60 to 0.70 from top to bottom. The heating profile employed is shown in Fig. 4.

5.1. Average powder properties

When the simulation was run according to Shinagawa's original formulation, the sample evolution shown in Fig. 5a resulted. In this case, what is really being simulated would be a structure akin to a laminate, since each horizontal layer is considered to be composed of uniformly sized particles. Consequently, the sintering rates vary strongly as a function of vertical position and the top region undergoes a more extensive amount of shrinkage. The non-uniformity of shrinkage rates stressed the material enough to induce the considerable warpage seen in Fig. 5a. The time labels in Fig. 5 refer to time elapsed after 3 h, at which time the sintering temperature reached 850 °C, considered to be sufficient heat to initiate the process. Experiments conducted in conjunction with the original model formulation showed that laminated structures did sinter to produce the warped shapes obtained by simulation [15].

5.2. Particle size distribution effects

When the effects of particle size distribution were incorporated into the simulation, the calculated output was considerably different compared to the previous case considering only average powder properties. In this case, the particle size distribution was inserted into the simulation as a local variable for each node in the solution space. The particle size distribution was input as a 200 point data set composed of radius and distribution frequency pairs. Calculations involving the distributions were done by spline fitting the data. Gaussian distributions centered on the same mean diameters as used in the average powder properties simulation were used. The standard deviations of the distributions were all set to 1 μm.

Fig. 5b shows the sintering behaviour of the samples modelled considering particle size distribution effects. These results show some key differences between the two different cases simulated. The main difference is that when accounting for particle size distribution effects, the structure is shown to undergo only minimal warpage. The case using average powder properties shows considerable warpage. In both cases, the overall sample shrinkage was similar, about 4% for the laminate case and around 5% for the case taking into account particle size distribution effects. The extent of shrinkage is reflected in the size of the structures shown in Fig. 5, but is not obvious for such a small percentage difference. A 5% shrinkage compares well to the 6–7% shrinkage observed with experimental samples. The overall shrinkage in the latter case is slightly higher owing to the accelerated sintering obtained when

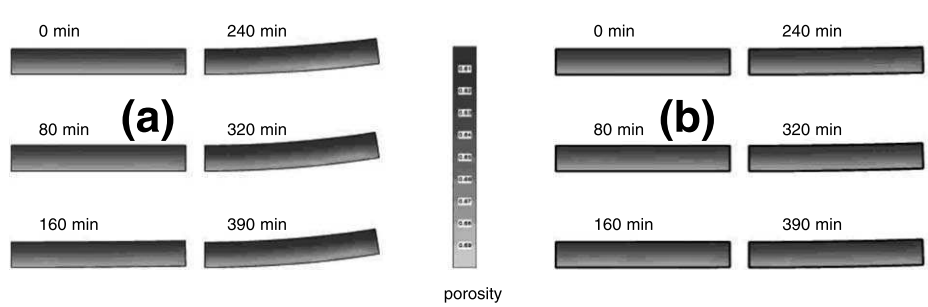

Fig. 5. Sample evolution over the sintering period. (a) Average powder properties considered in 10 layers. (b) Particle size distribution used as a field variable with initial conditions shown in Fig. 6.

particle size distribution effects are considered. In view of pair size effects discussed previously (i.e. Fig. 2), the acceleration in sintering would be more pronounced for a broad distribution with a larger mean diameter. In this way, the sintering rate is accelerated more due to particle size distribution effects towards the bottom of the structure, counterbalancing mean diameter effects, so that the net effect is a flatter sintered structure. This result is indeed obtained experimentally when samples of functionally gradient porous alumina made by sedimentation from a metastable colloidal state are sintered. Thus, the effect of a broad particle size distribution in the sample microstructure is to make the sintering rates more uniform throughout the gradient structure. Fig. 6 shows the particle size distributions at each of the 10 vertical center positions in the structure, and their evolution according to Eq. (10) over the course of the sinter. It can be seen that the fines are consumed by the coarser particles, and that the distributions broaden and drift to larger mean diameters with time. This behaviour is more pronounced for the particles which were finer to begin with, such that the net effect is to lessen differential shrinkage rates within the structure as time progresses. A numerical simulation of pore size distribution under constrained sintering of viscous material by Scherer [30] shows a very parallel type of evolution over time. This result is consistent with the present simulation in that particle and pore size distributions would evolve in the same functional manner.

The present formulation models the effect of a broad particle size distribution on the sintering behaviour of a porous body, and illuminates in a novel way how these particle size distribution effects are instrumental in minimizing sample warpage. For future work, the simulation will be run with measured data corresponding to physical samples in order to refine its numerical accuracy and precision. Such exploration should provide insight into correlations between porosity and grain size such as given by Eq. (4).

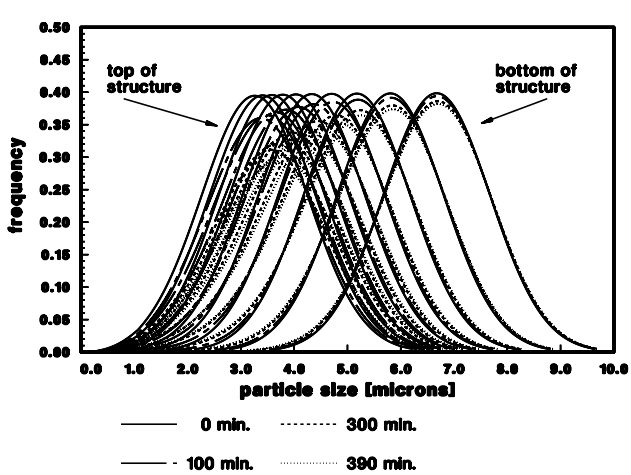

Fig. 6. Particle size distribution evolution for grid center point at same time intervals as given in Fig. 5.

6. Conclusions

Upon formulation and numerical implementation of a model designed to demonstrate the effects of local particle size distribution effects in a porous asymmetric ceramic structure, it can be said that these effects account for observed sintering behaviour in real and substantial ways. Compared to an asymmetric structure formed by lamination of uniform layers, a structure with a broad range of powder sizes and a continuously increasing mean powder diameter from top to bottom, sinters with considerably less warpage. These predictions correspond to the qualitative results obtained when physical samples with such characteristics are sintered. The presence of fines throughout the compact produces a sintered piece which fuses at lower temperatures and with less warpage. Thus, accounting for the particle size distribution as a field variable more realistically simulates the sintering result of functionally gradient materials prepared by colloidally metastable sedimentation. For future work, this simulation tool will prove valuable in understanding microstructural effects on sintering behaviour, and ultimately can aid in fabrication parameter optimization.

References

[1] K. Darcovich, C.R. Cloutier, J. Am. Cer. Soc. 82 (8) (1999) 2079.
[2] K. Darcovich, M.E. Price, Microstructure processing for asymmetric ceramic membrane substrates, in: A.G. Fane (Ed.), Proceedings of the International Membrane Science and Technology Conference—IMSTEC'96, Sydney, Australia, November 12–14, 1996, pp. 164–166.
[3] K. Darcovich, M.E. Price, J. Can. Cer. Soc. 66 (2) (1997) 146–151.
[4] M. Abouaf, J.L. Chenot, G. Raisson, P. Baudin, Int. J. Num. Meth. Eng. 25 (1988) 191–212.
[5] H. Reidel, D. Meyer, J. Svoboda, H. Zipse, Int. J. Refractory Met. Hard Mater. 12 (1993–1994) 55–60.
[6] A. Jagota, G.W. Scherer, J. Am. Cer. Soc. 78 (3) (1995) 521–528.
[7] Z.Z. Du, A.C.F. Cocks, Acta Metall. Mater. 40 (8) (1992) 1969–1979.
[8] R.M. McMeeking, L.T. Kuhn, Acta Metall. Mater. 40 (5) (1992) 961–969.
[9] K. Shinagawa, JSME Int. J. Ser. A 39 (4) (1996) 565–572.
[10] K. Shinagawa, Comp. Mater. Sci. 13 (1999) 276–285.
[11] M.F. Ashby, HIP 6.0 Background Reading, Eng. Department, University of Cambridge, 1990.
[12] J. Svoboda, H. Riedel, H. Zipse, Acta Metall. Mater. 42 (2) (1994) 435–443.
[13] M. Gasik, Comp. Mater. Sci. 13 (1998) 42–55.
[14] T. Moritz, H. Riedel, G. Werner, G. Tomandl, J. Mater. Sci. 35 (2000) 2235–2240.
[15] K. Shinagawa, Y. Hirashima, JSME Int. J. Ser. A 42 (1) (1999) 17–24.

[16] F. Parhami, R.M. McMeeking, Mech. Mater. 27 (1998) 111–124.
[17] S. Shima, M. Oyane, Int. J. Mech. Sci. 18 (1976) 285–291.
[18] R.L. Coble, J. Appl. Phys. 34 (1963) 1679–1682.
[19] R.M. Cannon, W.H. Rhodes, A.H. Heuer, J. Am. Cer. Soc. 63 (1–2) (1980) 46–53.
[20] W.D. Kingery, J. Am. Cer. Soc. 37 (2) (1954) 42–45.
[21] S. Sivakumar, Pradip, P.C. Kapur, S.G. Malghan, Colloids Surf. A: Physiochem. Eng. Aspects 133 (1998) 173–182.
[22] H.M. Hulbert, S. Katz, Chem. Eng. Sci. 19 (1964) 555–574.
[23] J.-M. Ting, R.Y. Lin, J. Mater. Sci. 30 (1995) 2382–2389.
[24] G.W. Greenwood, Particle Coarsening, in: The Mechanism of Phase Transformations in Crystalline Solids, Institute of Metals, Monograph and Report Series, No. 33, 1969, pp. 103–110.
[25] J. Pan, H. Le, S. Kuchernko, J.A. Yeomans, Acta Mater. 46 (13) (1998) 4671–4690.
[26] M. Suzuki, T. Oshima, Powder Technol. 44 (1985) 213–218.
[27] E. Arzt, Acta Metall. 30 (1982) 1883–1890.
[28] M. Miyayama, K. Koumoto, H. Yanagida, Engineering properties of single oxides, in: S.J. Schneider, Jr. (Ed.), Engineered Materials Handbook, vol. 4, ASM International, Ohio, 1991, pp. 748–757.
[29] T. Nishijima, T. Kawada, A. Ishihata, J. Am. Cer. Soc. 48 (1965) 31–34.
[30] G.W. Scherer, J. Am. Cer. Soc. 81 (1) (1998) 49–54.